Enhanced hydrophobicity and volatility of submicron aerosols under severe emission control conditions in Beijing

Yuying Wang[1], Fang Zhang[1], Zhanqing Li[1,2], Haobo Tan[3], Hanbing Xu[4], Jingye Ren[1], Jian Zhao[5,6], Wei Du[5,6], Yele Sun[5,6]

[1]College of Global Change and Earth System Science, Beijing Normal University, Beijing 100875, China

[2]Department of Atmospheric and Oceanic Sciences and ESSIC, University of Maryland, College Park, Maryland, USA

[3]Key Laboratory of Regional Numerical Weather Prediction, Institute of Tropical and Marine Meteorology, China Meteorological Administration, Guangzhou 510080, China

[4]Shared Experimental Education Center, Sun Yat-sen University, Guangzhou 510275, China

[5]State Key Laboratory of Atmospheric Boundary Layer Physics and Atmospheric Chemistry, Institute of Atmospheric Physics, Chinese Academy of Sciences, Beijing 100029, China

[6]College of Earth Sciences, University of Chinese Academy of Sciences, Beijing 100049, China

Correspondence to: Fang Zhang (fang.zhang@bnu.edu.cn), Zhanqing Li (zli@atmos.umd.edu)

Abstract. A series of strict emission control measures were implemented in Beijing and the surrounding seven provinces to ensure good air quality during the 2015 China Victory Day parade, rendering a unique opportunity to investigate anthropogenic impact of aerosol properties. Submicron aerosol hygroscopicity and volatility were measured during and after the control period using a hygroscopic and volatile tandem differential mobility analyzer (H/V-TDMA) system. Three periods, namely, the control clean period (Clean1), the non-control clean period (Clean2), and the non-control pollution period (Pollution), were selected to study the effect of the emission control measures on aerosol hygroscopicity and volatility. Aerosol particles became more hydrophobic and volatile due to the emission control measures. The hygroscopicity parameter (κ) of 40–200 nm particles decreased by 32.0 %–8.5 % during the Clean1 period relative to the Clean2 period, while the volatile shrink factor (SF) of 40–300 nm particles decreased by 7.5 %–10.5 %. The emission controls also changed the diurnal variation patterns of both the probability density function of κ (κ-PDF) and the probability density function of SF (SF-PDF). During Clean1 the κ-PDF showed one nearly-hydrophobic (NH) mode for particles in the nucleation mode, which was likely due to the dramatic reduction in industrial emissions of inorganic trace gases. Compared to the Pollution period, particles observed during the Clean1 and Clean2 periods exhibited a more significant non-volatile (NV) mode throughout the day, suggesting a more externally-mixed state particularly for the 150 nm particles. Aerosol hygroscopicities increased as particle sizes increased, with the greatest increases seen during the Pollution period. Accordingly, the aerosol volatility became weaker (i.e., SF

49   increased) as particle sizes increased during the Clean1 and Clean2 periods, but no

50   apparent trend was observed during the Pollution period. Based on a correlation

51   analysis of the number fractions of NH and NV particles, we found that a higher number

52   fraction of hydrophobic and volatile particles during the emission control period.

53   1. Introduction

54   China, as the world's second largest economy, is facing severe air pollution

55   problems due to its rapid economic growth. This has led to highly elevated aerosol

56   concentrations, especially in urban regions such as Beijing, Shanghai, and Guangzhou

57   (Hsu et al., 2012; Huang et al., 2014). Every year, high levels of fine particulate matter

58   (PM) have caused many severe haze days in these regions, that may pose a great health

59   hazard and changes in the regional climate because of aerosol direct and indirect climate

60   effects (Z. Li et al., 2016; G. X. Wu et al., 2016). However, the pollution formation

61   mechanism and the climate effects of aerosols remain highly uncertain due to the highly

62   variable physical and chemical properties of aerosols, as well as complex mechanisms

63   that govern aerosol-climate interactions (Tao et al., 2012; Wang et al., 2014).

64   Aerosol hygroscopicity and volatility are two important physical properties

65   describing the process of haze formation and its effects on climate. Aerosol

66   hygroscopicity describes the interaction of aerosols and water vapor under sub- and

67   supersaturation conditions, and is a vital parameter to the aerosol life cycle, aerosol

68   activation ability, and aerosol direct and indirect climate effects (Swietlicki et al., 2008;

69   Tao et al., 2012; Bian et al., 2014). Aerosol volatility is a physical parameter correlated

70 with carbonaceous aerosols, commonly used to study the aerosol mixing state and aging

71 level (Wehner et al., 2009; S. L. Zhang et al., 2016). To date, there are many ways to

72 measure aerosol hygroscopicity and volatility, but the most popular one is the

73 Hygroscopic and Volatile Tandem Differential Mobility Analyzer (H/V-TDMA)

74 system because it can measure these properties in great detail (Swietlicki et al., 2008).

75   The Chinese government took many drastic measures to reduce the emissions of

76 air pollutants from industry, road traffic, and construction sites, especially during some

77 great events such as the 2008 Summer Olympic Games, the 2014 Asia-Pacific

78 Economic Cooperation. Swift and drastic improvement in air quality (Huang et al.,

79 2015; Shi et al., 2016) provide unique opportunities to investigate the effects of

80 emissions on air quality. To our knowledge, previous studies have usually focused on

81 aerosol chemistry, sources, and transport (Wang et al., 2010; Gao et al., 2011; Sun et

82 al., 2016b), but not on the effects of emission controls on aerosol hygroscopicity and

83 volatility. Due to the importance of the two factors on describing the process of haze

84 formation as well as the effect on climate, it is necessary to investigate the changes in

85 aerosol hygroscopicity and volatility when emission control measures are in place.

86   To guarantee good air quality in Beijing during the 2015 China Victory Day parade,

87 the Chinese government implemented much stricter emission control measures than

88 normally done in Beijing and the surrounding seven provinces from 20 August to 3

89 September. The control measures consisted of a ban on driving vehicles every other day,

90 shutting down or limiting factory production, stopping construction activities, and so

91 on. These emission control measures successfully ensured a continuous stretch of 15

92   days of blue sky, vividly named "Parade Blue" (H. Li et al., 2016). During and after the

93   parade emission control period, we conducted in situ measurements of submicron

94   aerosol chemical and physical properties in Beijing. Size-resolved chemical

95   compositions were also obtained (Zhao et al., 2017). The average PM less than 1 μm in

96   diameter (PM_1) concentration was 19.3 μg m^{-3} during the parade emission control

97   period, 57 % lower than that after the control period. All chemical species decreased

98   during the control period, but their decreasing percentages were different.

99   This study period is unique for investigating aerosol properties during low PM level

100   periods. This paper will further evaluate the impact of emission controls on the

101   hygroscopicity and volatility of submicron aerosols, which may bring some insight into

102   how to reduce pollution in the future. Furthermore, investigating aerosol hygroscopicity

103   and volatility with and without emission controls will help in understanding

104   environmental and climate changes in general. This paper is structured as follows.

105   Section 2 describes the instrumentation and data used, and section 3 introduces the

106   methods to data analysis. Aerosol hygroscopicity and volatility during different periods

107   were compared and discussed in section 4. Conclusions and summary are given in

108   section 5.

109   **2.   Experimental methods**

110   **2.1. Sampling site and meteorology**

111   The submicron aerosol hygroscopicity and volatility were measured in situ from

112   26 August to 7 October 2015 using the H/VTDMA system located at the Institute of

113   Atmospheric Physics (IAP), Chinese Academy of Sciences (39.97°N, 116.37°E), which

114   is located between the north 3rd and 4th ring road in northern Beijing. The sampling

115   instruments were put into a white container at ground level and an air conditioner was

116   used to maintain the temperature at 20–25° C inside the container. Meteorological

117   variables, including temperature (T), relative humidity (RH), wind speed (WS), and

118   wind direction (WD), were measured at different heights of a 325 m meteorological

119   tower, the tower located ~20 m west of the container. To eliminate the influence of

120   buildings on wind, we selected the 280-m wind direction and 8-m wind speed as

121   references in this study. Simultaneously, particle number concentrations (10–600 nm)

122   were also measured by a scanning mobility particle sizer (SMPS) located at the 260-m

123   level of the tower. The SMPS is equipped with a long differential mobility analyzer

124   (DMA, Model 3081A, TSI Inc.) and a condensation particle counter (CPC, Model 3775,

125   TSI Inc.). In addition, the measurement of aerosol chemical composition using a High-

126   Resolution Aerosol Mass Spectrometer (HR-AMS) and an Aerosol Chemical

127   Speciation Monitor (ACSM) were deployed at ground level and at the 260-m level of

128   the tower, respectively. The HR-AMS was situated in a sampling room located on the

129   rooftop of a two-story building (~8 m), ~25 m north from the container. An analysis of

130   the aerosol chemical composition has been done (Zhao et al., 2017).

131   **2.2. Instrumentation and operation**

132   The H/V-TDMA system developed by the Guangzhou Institute of Tropical and

133   Marine Meteorology (ITMM) was used to measure the submicron aerosol

134 hygroscopicity and volatility. The H-TDMA system (H-mode) shown in Figure 1

135 consists of four main parts: (1) a nafion dryer (Model PD-70T-24ss, Perma Pure Inc.,

136 USA) and a bipolar neutralizer (Kr85, TSI Inc.). The nafion dryer ensured that the RH

137 of the sample flow was below 20 % over the entire measurement period, and the bipolar

138 neutralizer was used to equilibrate the charge of particles (Wiedensohler, 1988); (2) the

139 first differential mobility analyzer (DMA$_1$, Model 3081L, TSI Inc.): The DMA$_1$ was

140 used to select quasi-monodisperse particles of a certain diameter through a fixed electric

141 voltage. The diameters selected were 40, 80, 110, 150, and 200 nm; (3) a nafion

142 humidifier (Model PD-70T-24ss, Perma Pure Inc., USA). The nafion humidifier was

143 used to humidify the aerosol flow from the DMA$_1$ to a defined RH. In the study, we set

144 RH to 90 %; (4) the second DMA (DMA$_2$, same model as the DMA$_1$) and a

145 condensation particle counter (CPC, Model 3772, TSI Inc.). The DMA$_2$ and the CPC

146 were used together to measure the number size distribution of the humidified particles.

147 An automated valve located between the DMA$_1$ and the nafion humidifier directly

148 connects the DMA$_1$ with the CPC. This can be used to measure the 10–400 nm particle

149 number size distribution (PNSD) by varying the electric voltage of the DMA$_1$. Details

150 about the design of the HTDMA system and its applications are given by Tan et al.

151 (2013a).

152 The design of the V-TDMA system (V-mode) is similar to that of the H-TDMA

153 system, except that the nafion humidifier in the V-TDMA system was replaced by a

154 heating tube that induces the evaporation of volatile materials. The heating tube was an

155 80-cm long stainless steel tube with an inner diameter of 8 mm. With a sample flow

156   rate of 1.0 L min^{-1}, its residence time (~2.4 s) in the heated section is sufficient for the

157   volatile materials to be effectively vaporized (Cheung et al., 2016). In this study, the

158   heating temperature was set to 300° C. The residual particles of volatile compounds at

159   this temperature, such as sulfates, nitrates, and most organics, are mainly refractory

160   non-volatile organic carbon (such as polymer-type organics), and sea salts (Philippin et

161   al., 2004; Wehner et al., 2009; Cheung et al., 2016; Ma et al., 2016). Particle were

162   measured at the diameters of 40, 80, 110, 150, 200 and 300 nm. The H/V-TDMA system

163   has been successfully used in previous studies (Tan et al., 2013b; Cheung et al., 2016;

164   Tan et al., 2016).

165   The hygroscopic growth factor (GF) at a given RH and the volatile shrink factor

166   (SF) at a certain temperature are defined as the ratio of the conditional diameter to the

167   dry diameter, with respect to RH and T, respectively:

168 $$GF = D_p(RH)/D_{0dry} , \qquad\qquad (1)$$

169 $$SF = D_p(T)/D_{0dry} . \qquad\qquad (2)$$

170 Here, $D_p(RH)$ refers to the particle diameter measured at RH = 90 %, $D_p(T)$ refers to

171   the particle diameter measured at T = 300° C, and D_{0dry} refers to the dry diameter set by

172   the DMA$_1$. The measured distribution function (MDF) versus GF or SF can be

173   calculated with the number concentration from CPC data downstream from the DMA$_1$

174   and the DMA$_2$. However, the MDF is a skewed and smoothed integral transformation

175   of the particles' actual growth/shrink factor probability density function (GF-PDF or

176   SF-PDF) due to the effect of the DMA diffusion transfer function (Swietlicki et al.,

177   2008; Gysel et al., 2009). In this study, the TDMAfit algorithm (Stolzenburg et al., 1988,

178   2008) was used to retrieve the GF-PDF and the SF-PDF. The TDMAfit algorithm

179   assumes that groups in the PDF following one or more lognormal distribution functions

180   (Gaussian shape), thus allowing for the possibility that particles of a given type are not

181   all identical.

182   **3. Data analysis**

183   **3.1. Hygroscopicity parameter**

184   According to the Köhler theory (Petters et al., 2007), the hygroscopicity parameter

185   κ can be used to depict the hygroscopicity of particles at different RHs. Using H-TDMA

186   data, κ is calculated as:

$$\kappa(\text{GF}, D_d) = (\text{GF}^3 - 1) \cdot \left[\frac{1}{\text{RH}} \exp\left(\frac{4\sigma_{s/a} M_w}{RT\rho_w D_d \text{GF}} \right) - 1 \right] \quad , \tag{3}$$

188   where RH is the default value of the H-TDMA, $\sigma_{s/a}$ is the surface tension of the

189   solution/air interface, M_w is the molecular weight of water, R is the universal gas

190   constant, T is the temperature, ρ_w is the density of water, D_d is the diameter of the

191   dry particles (equivalent to D_{0dry} as mentioned above), and GF from equation (1). In this

192   study, T used in the κ calculation is 23° C (the average temperature of the inner

193   container) and $\sigma_{s/a}$ is assumed to be the same as the surface tension of the pure

194   water/air interface (about 0.0723 N m^{-1} at 23° C).

195   **3.2. Statistics of κ-PDF and SF-PDF**

196   The probability distribution function of κ (κ-PDF, $c(\kappa, D_d)$) derived from the GF-

197   PDF was normalized as $\int c(\kappa, D_d)\, d\kappa = 1$. The ensemble mean hygroscopicity

198 parameter is then defined as the number-weighted mean GF of κ-PDF over the whole κ

199 range:

$$\kappa_{mean} = \int_0^\infty \kappa c(\kappa, D_d) d\kappa \qquad . \tag{4}$$

201 The standard deviation of κ-PDF is:

$$\sigma_{\kappa-PDF} = \left(\int_0^\infty (\kappa - \kappa_{mean})^2 c(\kappa, D_d) d\kappa \right)^{\frac{1}{2}} \qquad . \tag{5}$$

203 The calculated statistical parameters of SF-PDF ($c(SF, D_d)$) are similar to those of κ-

204 PDF, so SF can be used instead of κ and $c(SF, D_d)$ instead of $c(\kappa, D_d)$ in these

205 equations.

3.3. Classification of different hygroscopic and volatile groups

207   The mixing state of ambient aerosol particles is complex due to different sources,

208 different aging processes, and so on. Different hygroscopic and volatile groups had been

209 used around the Beijing region using H-TDMAs and V-TDMAs (Massling et al., 2009;

210 Liu et al., 2011; S. L. Zhang et al., 2016). Based on previous studies and our

211 measurements (Fig. S1), ambient aerosol particles were classified into three

212 hygroscopic groups and three volatile groups, where κ and SF are used here to define

213 the boundaries for each group:

214   Nearly-Hydrophobic, NH: $\kappa < 0.1$;

215   Less-Hygroscopic, LH: $0.1 \leq \kappa < 0.2$;

216   More-Hygroscopic, MH: $0.2 \leq \kappa$;

217   Non-Volatile, NV: $SF \geq 0.88$;

218   Slight-Volatile, SV: $0.88 > SF \geq 0.55$;

219   Very-Volatile, VV: SF $<$ 0.55.

220   The number fraction (NF) for each hygroscopic group with the boundary of [a, b]

221   is defined as:

222                    $$NF = \int_a^b c(\kappa, Dp)d\kappa \quad .$$ (6)

223   The number fraction of each volatile group also can be calculated using a similar

224   equation.

225   **4. Results and discussion**

226   **4.1. Overview of measurements**

227   **4.1.1. Meteorological conditions during the sampling period**

228   Air quality has a strong correlation with local wind direction in Beijing. Previous

229   studies have shown that high PM concentrations usually correspond to southerly winds,

230   while low PM concentration are generally related to northerly winds, because there

231   were more high concentration air pollutants from source locations south of the Beijing

232   area (Wehner et al., 2008; Wang et al., 2010; Gao et al., 2011). Figure 2 displays time

233   series of WD at 280 m, WS at 8 m, ambient T, and RH. During the emission control

234   period, the prevailing winds were northerly, except for the period from 29 August to 30

235   August due to the influence of accumulated precipitation. During the non-control period,

236   the prevailing winds changed due to the influence of weather systems. Two cold fronts

237   passed on two different days, i.e., on the night of 9 September and in the early morning

238   of 30 September. During these frontal passages, the prevailing winds were northerly,

239   but on other days, the prevailing winds were southerly and the meteorological

240 parameters showed obvious diurnal cycle patterns. Over the measurement period, the

241 average ambient T and RH were 21.9°C and 62.4 %, respectively.

242 **4.1.2. Time series of κ-PDF and SF-PDF, and the division of clean and pollution**

243   **periods**

244   Figure 3 shows the time series of 10–400 nm particle mass concentrations (PM$_{10-}$

245 $_{400\,nm}$) derived from PNSD measurements and the time series of κ-PDF and SF-PDF

246 with 40 nm and 150 nm particles as examples. Particles with D$_p$ equal to 40 nm

247 represent local-impacted particles and particles with D$_p$ equal to 150 nm represent

248 regional-transport particles. Several haze events during the non-control period can be

249 seen from the time series of PM$_{10-400\,nm}$, which shows the rapid accumulation of particle

250 mass concentration. Based on mass concentrations and weather conditions, we selected

251 several clean and pollution periods to study the differences in aerosol hygroscopicity

252 and volatility for two different cases (Fig. 3). To further study the effect of emission

253 controls, we divided the clean period into two periods: Clean1 (control clean period)

254 and Clean2 (non-control clean period). During the Clean1, Clean2, and Pollution

255 periods, the average PM$_{10-400\,nm}$ was 6.9±2.8, 6.0±4.2, and 51.0±25.6 μg m^{-3},

256 respectively. There was no significant precipitation during the three selected periods.

257 The time series of κ-PDF and SF-PDF (Fig. 3b–e) showed evident changes and

258 fluctuations in the measurements. The prominent differences in κ-PDF and SF-PDF

259 during the three periods will be discussed in the following sections.

260   A wind rose diagram (Fig. S2) was used to compare winds during the different

261 periods. During the Clean1 and Clean2 periods, wind directions were similar, mainly

262 from the north and northwest. During the Pollution period, the wind direction had the

263 characteristics of mountain-valley breezes where the wind direction changed routinely

264 at midnight and changed the wind direction from southerly to northerly (Fig. 2). The

265 change in wind direction at night would reduce pollution in the short term (Sun et al.,

266 2016b). Even so, the prevailing wind direction was southerly during the Pollution

267 period (Fig. S2), which was favorable for the transport of pollutants from the more

268 populated and more industrialized south and southeast to Beijing. The mean WS and

269 RH were similar during all periods, but the mean temperature during the Clean2 period

270 was lower than during the other periods due to the influence of cold fronts (Table S1).

271 In summary, the meteorological parameters of the Clean1 and Clean2 cases were similar

272 expect for the ambient T. This provided the opportunity to compare the differences in

273 aerosol properties between control and non-control periods. The high level of PM

274 during the Pollution case can also provide a good opportunity to compare differences

275 between clean and polluted environments.

276 **4.2.Diurnal variation**

277 **4.2.1.   Diurnal variation in the aerosol size distribution**

278   Figure 4a shows the diurnal variation in total number concentration of 10–400 nm

279 particles ($N_{10–400 \text{ nm}}$). In general, $N_{10–400 \text{ nm}}$ is higher at night and lower during the day

280 due to the influence of changes in the planetary boundary layer (PBL). However, a

281 significant peak in $N_{10–400 \text{ nm}}$ is also seen at noontime because of new particle formation

282 (NPF) events (Fig. S3). NPF started at about 0900 local time (LT) during the Clean1

283 and Clean2 periods. During the Clean1 period, the $N_{10-400\,nm}$ peak was lower than that

284 observed during the Clean2 period, and the peak in the Clean1 case appeared two hours

285 earlier than that in the Clean2 case (1200 LT during Clean1 and 1400 LT during Clean2).

286 This illustrates that the strength of the NPF was weaker during the Clean1 period than

287 during the Clean2 period, and that it was likely related to the decrease in precursors

288 during the Clean1 period. H. Li et al. (2016) have reported that during the parade control

289 period, the precursors SO_2, NO_x, and volatile organic compounds (VOCs) decreased by

290 36.5 %, 49.9 %, and 32.4 %, respectively. The relatively higher ambient temperature

291 during the Clean1 period was also unfavorable for NPF (Kulmala et al., 2004).

292   Figure 4b compares diurnal variations in total mass concentration of 10–400 nm

293 particles ($PM_{10-400\,nm}$) during the three periods. No clear increase in $PM_{10-400\,nm}$ is seen

294 while $N_{10-400\,nm}$ sharply increases during the Clean1 and Clean2 daytime periods. This

295 is because the D_p for most particles was less than 100 nm, which contributed little to

296 $PM_{10-400\,nm}$. During the Clean1 and Clean2 periods, $PM_{10-400\,nm}$ had an obvious diurnal

297 variation, which could be attributed to the evolution of the PBL. As is known, the lower

298 PBL at night aids in the accumulation of pollutants (Achtert et al., 2009). However, this

299 effect was weak in the pollution case because of the change in wind direction from

300 southerly to northerly at midnight, which could partly offset the influence of the PBL.

301 **4.2.2. Diurnal variation in aerosol hygroscopicity**

302   Figure 5a shows the diurnal variation in size-resolved κ_{mean} during the three periods.

303 κ_{mean} shows a peak during daytime, and is always higher than that observed during

304 nighttime. This is because more highly aged particles due to photochemical reactions

305 cause the increase in κ_{mean} during daytime. In the evening, thermal inversion would cap

306 the ground level and a number of low hygroscopic primary particles (like black carbon,

307 BC) emitted from local diesel trucks and heavy-duty vehicles results in the decrease in

308 κ_{mean} during nighttime (Liu et al., 2011; S. L. Zhang et al., 2016). During the Clean2

309 period, there is another obvious peak at about 0300 LT in the early morning, likely

310 related to the increase in nitrate. Because there was a large amount of NO_x emitted from

311 traffic sources in the evening during the non-control period, with the PBL height

312 reduction and ambient temperature decrease, NO_x could be transformed into

313 hydrophilic nitrate rapidly through NO_3 and N_2O_5 (Dall'Osto et al., 2009). This was

314 also verified from comparisons of the nitrate diurnal cycle with and without emission

315 controls (Zhao et al., 2017).

316   Figure 5b shows the diurnal variation in κ-PDF for particles with D_p equal to 40

317 nm (i.e., local-impacted particles) during the three periods. During the Clean1 period,

318 the κ-PDF has a quasi-unimodal shape (only in the hydrophobic mode). During NPF

319 events, κ_{mean} increases slightly, indicating that 40-nm particles from local sources were

320 always hydrophobic and a very small amount of hygroscopic particles were produced

321 through the nucleation and growth from gaseous precursors. This is likely because the

322 secondary formation of hydrophilic sulfate and nitrate was suppressed due to low

323 concentrations of SO_2 and NO_X during the parade control period (H. Li et al., 2016).

324 Most of the new particles should consist of less hygroscopic organics that are formed

325 by oxidation and condensation of VOCs. By contrast, during the Clean2 period, the κ-

326 PDF with D_p of 40 nm shows either a bimodal or quasi-trimodal distribution and

327 exhibits a large diurnal variation during the day. Interestingly, when the NPF event

328 occurred at about 0900 LT, the number fraction of the hydrophobic mode quickly

329 decreased and the hydrophilic mode increased (Fig. 5b), suggesting the conversion of

330 externally mixed particles to internally mixed particles due to the species condensation

331 (sulfate, nitrate and organics) from the photochemical reaction of SO_2, NO_x and VOCs.

332 A similar phenomenon was also observed by Z.J. Wu et al. (2016). For the Clean1 case,

333 much less of these gases were in the atmosphere due to the emission control. Around

334 1700 LT, the fraction of hydrophobic mode particles increased again, mainly due to

335 substantial traffic emissions at rush hour. However, during the Pollution period, the κ-

336 PDF shows a bimodal shape during the day. The hydrophilic mode becomes stronger in

337 the early morning and in the afternoon, which is attributed to the NO_x heterogeneous

338 reactions at night, and the aging and growth of pre-existing particles during the day.

339   In summary, the diurnal variations in κ-PDF for 40-nm particles were significantly

340 different during the three periods and the emission control appeared to change the

341 diurnal pattern of κ-PDF, mainly due to the decrease in gas precursors, like SO_2 and

342 NO_x, the reduction of which will suppress the formation of hydrophilic matter.

343   However, the κ-PDF for 150-nm D_p particles (i.e., regional-transport particles) had

344 a similar diurnal variation pattern during the three periods (Fig. 5c) and showed NH

345 and MH modes. The number fraction of the MH mode increased significantly during

346 daytime. There are different reasons for the diurnal variations. One reason is that during

347 daytime, strong photochemistry can produce a large number of condensable vapors,

such as sulfuric acid and secondary organic species, which can condense onto pre-existing particles and enhance their water absorbing capacity (Z. J. Wu et al., 2016). Another reason is that when the sun rises, the PBL height increases and older particles are well-mixed, making them more hydrophilic (S. L. Zhang et al., 2016). However, the MH mode is much more evident for the Pollution case and may be related to the higher mass fractions of inorganic salts and more internal-mixed particles during the Pollution period.

4.2.3. Diurnal variation in aerosol volatility

Figure 6a shows the diurnal variation in SF_{mean}, which shows similar trends for all three cases, with the lowest SF_{mean} in the afternoon (1200–1500 LT) and the highest SF_{mean} in the morning (0700–0900 LT) for all particles with D_p ranging from 40-300 nm. The diurnal variations illustrate that particles had a higher volatility during the day than at night. This feature is more obvious for those small particles observed during the Clean1 period. During the Clean1 period, particle volatility increased dramatically (i.e., SF_{mean} decreased) along with the occurrence of NPF events, suggesting that the earliest newly-formed matter (before ~1200 LT) were always volatile at 300° C. As stated previously, during the Clean1 period VOCs has a weaker decrease than SO_2 and NOx, this would lead to more VOC-formed organic particles formed, which are normally highly volatile. Therefore, the highest volatility was observed during the Clean1 period. Wehner et al. (2009) also showed that ~97 % of newly-formed particles are volatile because they are dominated by sulfate and organics. With the processes of particle aging,

369 collision, and growth, they then decrease in volatility (i.e., SF_{mean} increases). This is

370 because these processes can enhance the oxidative level of organics and there are more

371 refractory organics (like polymer-type organics) produced.

372   For 40-nm particles, the lowest SF_{mean} appeared two hours later during the Clean2

373 period (~1500 LT) than during the Clean1 period (~1300 LT). This is probably because

374 NPF lasted longer during the Clean2 period. For larger particles, the coating effect of

375 condensable vapors onto pre-existing particles was the major reason behind the

376 intensification of their volatility during NPF events (Wehner et al., 2009; Cheung et al.,

377 2016). The SF_{mean} decreased little compared to that for 40-nm particles. By comparison,

378 the diurnal variation in SF_{mean} for 40-nm particles during the Pollution period changed

379 more smoothly, likely because under a polluted environment, the mass fractions of all

380 chemical species were relatively stable (Sun et al., 2016a) and the particles were well-

381 mixed with highly aging levels.

382   Figure 6b and 6c show the diurnal variation in SF-PDF for 40 nm and 150 nm

383 particles. The SF-PDF normally has an NV mode and a SV or VV mode. The NV mode

384 consists of non-volatile particles, like BC particles, which do not shrink when aerosols

385 are heated. SV and VV modes suggest a mixture of volatile (e.g., organics) and non-

386 volatile matter that shrink when aerosols are heated (Kuhn et al., 2005). The two SF-

387 PDF modes suggest that the particles during the observed periods were mostly

388 externally-mixed. The 40-nm and 150-nm SF-PDF show similar diurnal patterns.

389 During daytime, active aging processes facilitated the mixing of primary particles with

390 secondary species, leading to the transformation of externally-mixed particles to

391 internally-mixed particles, and weakening the NV mode. In particular, this effect was

392 stronger during the Clean1 period than during the other periods. This may be due to the

393 reduction in emissions of soot particles during the control period. In the evening and

394 the early morning, the number fraction of NV-mode particles increased again because

395 a large amount of refractory particles (like BC) were emitted from traffic sources or

396 cooking, and then the slower particle aging and weaker vertical mixing made the

397 external-mixing BC accumulated (S. L. Zhang et al., 2016). The number fraction of

398 NV-mode 150-nm particles in the Clean1 case had a stronger increase than that of 40-

399 nm particles in the evening and early morning. This is because freshly emitted

400 refractory particles (like BC) are primarily within the 150 nm to 240 nm diameter range

401 (Levy et al., 2013). Furthermore, compared with the Pollution case, the number fraction

402 of NV-mode 150-nm particles are much higher during the Clean1 and Clean2 cases.

403 This may reflect the fact that soot particles in a polluted environment can be coated and

404 aged quickly through the heterogeneous reactions of VOCs and other precursor gases

405 (like SO_2, NO_x), which are usually present in extremely high concentrations during

406 polluted days in urban Beijing (Guo et al., 2014; Sun et al., 2016a).

407   Overall, the diurnal variation in aerosol volatility is different between clean and

408 polluted periods. NPF can enhance volatility through the formation of volatile matter

409 and the coating effect of condensation vapors. Particles observed during the control

410 period showed two significant NV and VV modes during the day, suggesting a more

411 externally-mixed state, particularly for the larger particles.

4.3. Size-resolved particle hygroscopic and volatile properties

412

413 Table 1 summarizes the size-resolved mean κ, the growth spread factor ($\sigma_{\kappa\text{-PDF}}$) of

414 κ-PDF, size-resolved SF during different periods, and the change in percentages of κ

415 and SF due to the emission control policy. The $\sigma_{\kappa\text{-PDF}}$, defined as the standard deviation

416 of κ-PDF, is an indication of the mixing state of aerosol particles. A higher $\sigma_{\kappa\text{-PDF}}$

417 generally suggests a higher degree of external mixing (Sjogren et al., 2008; Liu et al.,

418 2011; Jiang et al., 2016). Liu et al. (2011) chose $\sigma_{\kappa\text{-PDF}} = 0.08$ as the cut-off point for

419 high external mixing and quasi-internal mixing. In this study, $\sigma_{\kappa\text{-PDF}}$ always exceeds

420 0.08 but the 40-nm particles during the Clean1 period, indicating that the particle

421 population was more externally mixed in urban Beijing. The mean $\sigma_{\kappa\text{-PDF}}$ of 40-nm

422 particles during the Clean1 period is equal to 0.08, suggesting that during the control

423 period, 40-nm particles had a low degree of external mixing. This is also seen in the

424 quasi-unimodal distribution of 40-nm κ-PDF (Fig. 5b).

425 During the selected three periods, aerosol particles were more hygroscopic (i.e., κ

426 increased) with increase in particle size (Fig. 7a). The most significant trend is seen in

427 the Pollution case where κ increases from 0.16 to 0.42 when D_p changes from 40 nm to

428 200 nm, but only increases from 0.10 to 0.25 for the Clean1 case and from 0.14 to 0.28

429 for the Clean2 case. This is because particles with a larger size are usually composed

430 of more inorganic salts or oxidized organics, especially in a polluted environment

431 (Swietlicki et al., 2008; Achtert et al., 2009; Fors et al., 2011; Sun et al., 2016a).

432 Meanwhile, the increase in $\sigma_{\kappa\text{-PDF}}$ with the increase in particle size illustrates that there

433 were more external mixing particles with larger sizes (Table 1). Accordingly, aerosol

434   volatility became weaker (SF increased) as particle size increased during the Clean1

435   and Clean2 periods, but no apparent trend was observed for the Pollution period (Fig.

436   7b). This finding is consistent with that reported by Wehner et al. (2009).

437   Figure 6 also shows that all particles were less hygroscopic and more volatile

438   during the control Clean1 period than during the non-control Clean2 period, which can

439   also be seen from the variation in chemical composition. Based on HR-AMS

440   measurements, secondary inorganic aerosols (SIA) had larger decreases than organic

441   aerosols (OA) during the parade control period. The positive matrix factorization of OA

442   further illustrates that primary OA (POA) had similar decreases as secondary OA

443   (SOA). However, more-oxidized SOA had larger decreases than less-oxidized SOA

444   (Zhao et al., 2017). SIA is always more hydrophilic than OA and more-oxidized SOA

445   is also more hydrophilic than less-oxidized SOA (Jimenez et al., 2009; Chang et al.,

446   2010; Rickards et al., 2013; Zhang et al., 2014; F. Zhang et al., 2016). Therefore, the

447   increased fraction of POA emissions, but weakened age processing due to a sharp

448   reduction in SO_2 and NO_x, lead to particles being less hygroscopic during the control

449   period. Meanwhile, particles become relatively more volatile due to the high number of

450   POA particles because OA volatility is generally inversely correlated with the O:C ratio

451   (an indicator of oxidation state) (Jimenez et al., 2009).

452   To quantify the effects of emission control on aerosol hygroscopicity and volatility,

453   Table 1 also gives the change in percentages of κ and SF during the control Clean1

454   period compared with that during the non-control Clean2 period. Results show that κ

455   decreased by 32.0–8.5 % from 40 nm to 200 nm during the control period, with a more

456   significant reduction for small particles, while SF reduced by 7.5–10.5 % from 40 nm

457   to 300 nm. The significant decrease in aerosol hygroscopicity is favorable for

458   decreasing the aerosol water content, thus suppressing the evolution of regional air

459   pollution (like liquid-phase chemical reaction processes in the atmosphere) (Arellanes

460   et al., 2006; Ye et al., 2011; Bian et al., 2014), and eventually improving atmospheric

461   visibility.

462   In addition, because of the reduced hygroscopicity, fewer particles would be

463   activated as cloud condensation nuclei, which is a critical parameter in evaluating the

464   aerosol indirect effect. Thus, our study is important for investigating environmental and

465   climate changes, and should inspire both scientists and policy makers to think more

466   deeply about the issue of heavy air pollution in China.

467   **4.4. Relationship between nearly-hydrophobic and non-volatile particles**

468   For submicron particles, non-volatile (NV) part particles at 300°C were normally

469   the major nearly-hydrophobic (NH) part particles because both their main components

470   are soot particles (Massling et al., 2009; Wehner et al., 2009). S. L. Zhang et al. (2016)

471   compared the relationship between the number fraction of measured non-volatile

472   particles (NF_{NV}) and nearly hydrophobic (NF_{NH}) particles and found those two groups

473   are very likely to be dominated by the same component. In this study, we also analyze

474   the relationship of NF_{NH} and NF_{NV} particles as shown Fig. 8.

475   The results show that Aitken mode particles (40 nm and 80 nm) have a very weak

476   linear relationship between NF_{NH} and NF_{NV}, likely because Aitken mode particles are

477   not as aged. There are a large number of hydrophobic, but volatile, particles such as

478   POA and less-oxidized SOA. Accumulation mode particles (> 100 nm) show a

479   relatively better linear correlation between NF_{NH} and NF_{NV}, i.e., correlation

480   coefficients (R^2) are 0.26, 0.55, and 0.62 for 110, 150, and 200 nm particles,

481   respectively. The higher R^2 for the larger particles may arise because larger particles

482   are highly aged particles from cloud processes. Also, freshly emitted refractory and

483   hydrophobic matter is mostly in the accumulation mode (Levy et al., 2013). The best-

484   fit regression line for the accumulation mode particles is always lower than the 1:1 line.

485   This can be attributed not only to externally mixed SIA and volatile organics

486   (completely volatile), which are not taken into account for calculation, but also to that

487   some medium/high volatile organics are nearly-hydrophobic.

488   There were obvious differences in NF_{NH} and NF_{NV} during the three selected

489   periods. For the Clean1 and Clean2 cases, NF_{NH} and NF_{NV} were larger than those

490   obtained for the Pollution case, but more scatter was seen. This is likely related to the

491   influence of NPF events, during which secondary aerosol material had more complex

492   chemical compositions due to the different sources of precursors. A higher NF_{NH}/NF_{NV}

493   ratio was seen during the Clean1 period than during the other two periods, illustrating

494   that a higher number fraction of hydrophobic and volatile particles during the control

495   period.

496

5. Conclusions and Summary

In this study, a H/V-TDMA system was used to measure submicron aerosol hygroscopic and volatile properties in Beijing during and after the parade emission control period. Three periods, namely, the control clean period (Clean1), the non-control clean period (Clean2), and the non-control pollution period (Pollution), were selected to study the effect of emission control on aerosol hygroscopicity and volatility.

When emission control measures were in place, particles became more hydrophobic and volatile compared to particles in the non-control period. The κ of 40–200 nm particles decreased by 32.0–8.5 % during the Clean1 period relative to the Clean2 period, while SF of 40–300 nm particles decreased by 7.5–10.5 %. The diurnal variations of κ-PDF were significantly different during the three selected periods, especially for small particles. During the Clean1 period, the κ-PDF of 40-nm particles always showed a quasi-unimodal distribution and had a weaker diurnal variation than that observed during the Clean2 period. This demonstrates that emission control measures can change the diurnal variation pattern of κ-PDF due to the reduction in gas precursors like SO_2 and NO_x, which suppresses the formation of hydrophilic matter. The diurnal variation in aerosol volatility was different between clean and polluted periods. NPF appears to enhance aerosol volatility through the formation of volatile matter and the coating effect of condensable vapors. The particles observed during the control period showed two significant modes during the day, i.e., NV and VV modes, and a more externally-mixed state particularly for larger particles.

Aerosol particles became more hygroscopic (i.e., κ increases) as the particle size

519   increased during the three periods. The trend was greatest for the Pollution case where

520   κ increased from 0.16 to 0.42 when D_p changed from 40 nm to 200 nm, but only

521   increased from 0.10 to 0.25 for the Clean1 case and from 0.14 to 0.28 for the Clean2

522   case. Meanwhile, the increase in $\sigma_{\kappa\text{-PDF}}$ (i.e., the standard deviation of κ-PDF) with the

523   increase in particle size also illustrates that there were more external mixing particles

524   with larger sizes. Accordingly, aerosol volatility became weaker (SF increased) as

525   particle size increased during the Clean1 and Clean2 periods, but no apparent trend was

526   observed for the Pollution period.

527   Our results suggest that emission control measures weaken submicron aerosol

528   hygroscopicity, and that aerosol particles are more hygroscopic in a polluted

529   environment. The significant decrease in aerosol hygroscopicity is favorable for

530   suppressing the evolution of regional air pollution. In addition, because of the reduced

531   hygroscopicity, fewer particles would be activated as could condensation nuclei, which

532   is a critical parameter in evaluating the aerosol indirect effect. Thus, our study is

533   important for investigating environmental and climate changes, and should inspire both

534   scientists and policy makers to think more deeply about the issue of heavy air pollution

535   in China from a broader perspective.

536

537   **Acknowledgements**

538   This work was funded by the NSFC research project (Grant No. 41675141,

539   91544217, 41375156), the National Basic Research Program of China '973' (Grant

540   No. 2013CB955800), and the NSFC-TAMU Collaborative Research Grant Program

541   (Grant No. 4141101031). We also thank all participants in the field campaign for their

542   tireless work and co-operation.

543

544   **References:**

545   Achtert P., Birmili W., Nowak A., Wehner B., Wiedensohler A., Takegawa N., Kondo Y., Miyazaki Y.,
546   Hu M. and Zhu T.: Hygroscopic growth of tropospheric particle number size distributions over the
547   North China Plain, J. Geophys. Res., 114, D2, doi:10.1029/2008jd010921, 2009.

548   Arellanes C., Paulson S.E., Fine P.M. and Sioutas C.: Exceeding of Henry's Law by Hydrogen Peroxide
549   Associated with Urban Aerosols, Environ. Sci. Technol., 40, 4859-4866, 2006.

550   Bian Y.X., Zhao C.S., Ma N., Chen J. and Xu W.Y.: A study of aerosol liquid water content based on
551   hygroscopicity measurements at high relative humidity in the North China Plain, Atmos. Chem. Phys.,
552   14, 6417-6426, 2014.

553   Chang R., Slowik J.G., Shantz N.C., Vlasenko A., Liggio J., Sjostedt S.J., Leaitch W.R. and Abbatt J.:
554   The hygroscopicity parameter (kappa) of ambient organic aerosol at a field site subject to biogenic
555   and anthropogenic influences: relationship to degree of aerosol oxidation, Atmos. Chem. Phys., 10,
556   5047-5064, 2010.

557   Cheung H.H., Tan H., Xu H., Li F., Wu C., Yu J.Z. and Chan C.K.: Measurements of non-volatile
558   aerosols with a VTDMA and their correlations with carbonaceous aerosols in Guangzhou, China,
559   Atmos. Chem. Phys., 16, 8431-8446, 2016.

560   Dall'Osto M., Harrison R.M., Coe H., Williams P.I. and Allan J.D.: Real time chemical characterization
561   of local and regional nitrate aerosols, Atmos. Chem. Phys., 9, 3709-3720, 2009.

562   Fors E.O., Swietlicki E., Svenningsson B. and Kristensson A.: Hygroscopic properties of the ambient
563   aerosol in southern Sweden – a two year study, Atmos. Chem. Phys., 11, 8343-8361, 2011.

564   Gao Y., Liu X., Zhao C. and Zhang M.: Emission controls versus meteorological conditions in
565   determining aerosol concentrations in Beijing during the 2008 Olympic Games, Atmos. Chem. Phys.,
566   11, 12437-12451, 2011.

567   Guo S., Hu M., Zamora M.L., Peng J., Shang D., Zheng J., Du Z., Wu Z., Shao M., Zeng L., Molina M.J.
568   and Zhang R.: Elucidating severe urban haze formation in China, Proc Natl Acad Sci USA, 111,
569   17373-17378, doi:10.1073/pnas.1419604111, 2014.

570   Gysel M., McFiggans G.B. and Coe H.: Inversion of tandem differential mobility analyser (TDMA)
571   measurements, J. Aerosol Sci., 40, 134-151, doi:10.1016/j.jaerosci.2008.07.013, 2009.

572   Hsu N.C., Gautam R., Sayer A.M., Bettenhausen C., Li C., Jeong M.J., Tsay S.C. and Holben B.N.:
573   Global and regional trends of aerosol optical depth over land and ocean using SeaWiFS measurements
574   from 1997 to 2010, Atmos. Chem. Phys., 12, 8037-8053, doi:10.5194/acp-12-8037-2012, 2012.

575   Huang K., Zhang X. and Lin Y.: The "APEC Blue" phenomenon: Regional emission control effects
576   observed from space, Atmos. Res., 164, 65-75, 2015.

577   Huang R., Zhang Y., Bozzetti C., Ho K., Cao J., Han Y., Daellenbach K.R., Slowik J.G., Platt S.M.,
578   Canonaco F., Zotter P., Wolf R., Pieber S.M., Bruns E.A., Crippa M., Ciarelli G., Piazzalunga A.,
579   Schwikowski M., Abbaszade G., Schnelle-Kreis J., Zimmermann R., An Z., Szidat S., Baltensperger
580   U., Haddad I.E. and Prévôt A.S.H.: High secondary aerosol contribution to particulate pollution during
581   haze events in China, Nature, doi:10.1038/nature13774, 2014.

582   Jiang R.X., Tan H.B., Tang L.L., Cai M.F., Yin Y., Li F., Liu L., Xu H.B., Chan P.W., Deng X.J. and

583 Wu D.: Comparison of aerosol hygroscopicity and mixing state between winter and summer seasons
584 in Pearl River Delta region, China, Atmos. Res., 169, 160-170, 2016.

585 Jimenez J.L., Canagaratna M.R., Donahue N.M., Prevot A., Zhang Q., Kroll J.H., DeCarlo P.F., Allan
586 J.D., Coe H. and Ng N.L.: Evolution of organic aerosols in the atmosphere, Science, 326, 1525-1529,
587 2009.

588 Kuhn T., Biswas S. and Sioutas C.: Diurnal and seasonal characteristics of particle volatility and chemical
589 composition in the vicinity of a light-duty vehicle freeway, Atmos. Environ., 39, 7154-7166,
590 doi:10.1016/j.atmosenv.2005.08.025, 2005.

591 Kulmala M., Vehkamäki H., Petäjä T., Dal Maso M., Lauri A., Kerminen V.M., Birmili W. and McMurry
592 P.H.: Formation and growth rates of ultrafine atmospheric particles: a review of observations, J.
593 Aerosol Sci., 35, 143-176, doi:10.1016/j.jaerosci.2003.10.003, 2004.

594 Levy M.E., Zhang R., Khalizov A.F., Zheng J., Collins D.R., Glen C.R., Yuan W., Yu X.Y., Winston L.
595 and Jayne J.T.: Measurements of submicron aerosols in Houston, Texas during the 2009 SHARP field
596 campaign, Journal of Geophysical Research Atmospheres, 118, 10518-10534, 2013.

597 Li H., Zhang Q., Duan F., Zheng B. and He K.: The "Parade Blue": effects of short-term emission control
598 on aerosol chemistry, Faraday Discuss., 189, 317-335, 2016.

599 Li Z., Lau W.M., Ramanathan V., Wu G., Ding Y., Manoj M.G., Liu J., Qian Y., Li J. and Zhou T.:
600 Aerosol and monsoon climate interactions over Asia, Rev. Geophys., 2016.

601 Liu P.F., Zhao C.S., Bel T.G., Hallbauer E., Nowak A., Ran L., Xu W.Y., Deng Z.Z., Ma N.,
602 Mildenberger K., Henning S., Stratmann F. and Wiedensohler A.: Hygroscopic properties of aerosol
603 particles at high relative humidity and their diurnal variations in the North China Plain, Atmos. Chem.
604 Phys., 11, 3479-3494, 2011.

605 Ma N., Zhao C., Tao J., Wu Z., Kecorius S., Wang Z., Groess J., Liu H., Bian Y., Kuang Y., Teich M.,
606 Spindler G., Mueller K., van Pinxteren D., Herrmann H., Hu M. and Wiedensohler A.: Variation of
607 CCN activity during new particle formation events in the North China Plain, Atmos. Chem. Phys., 16,
608 8593-8607, doi:10.5194/acp-16-8593-2016, 2016.

609 Massling A., Stock M., Wehner B., Wu Z.J., Hu M., Brüggemann E., Gnauk T., Herrmann H. and
610 Wiedensohler A.: Size segregated water uptake of the urban submicrometer aerosol in Beijing, Atmos.
611 Environ., 43, 1578-1589, 2009.

612 Petters M.D. and Kreidenweis S.M.: A single parameter representation of hygroscopic growth and cloud
613 condensation nucleus activity, Atmos. Chem. Phys., 7, 1961-1971, 2007.

614 Philippin S., Wiedensohler A. and Stratmann F.: Measurements of non-volatile fractions of pollution
615 aerosols with an eight-tube volatility tandem differential mobility analyzer (VTDMA-8), J. Aerosol
616 Sci., 35, 185-203, 2004.

617 Rickards A.M.J., Miles R.E.H., Davies J.F., Marshall F.H. and Reid J.P.: Measurements of the sensitivity
618 of aerosol hygroscopicity and the κ parameter to the O/C ratio., J. Phys. Chem. A, 117, 14120-14131,
619 2013.

620 Shi H., Wang Y., Chen J. and Huisingh D.: Preventing smog crises in China and globally, J. Clean. Prod.,
621 112, 1261-1271, 2016.

622 Sjogren S., Gysel M., Weingartner E., Alfarra M.R., Duplissy J., Cozic J., Crosier J., Coe H. and
623 Baltensperger U.: Hygroscopicity of the submicrometer aerosol at the high-alpine site Jungfraujoch,
624 3580 m asl, Switzerland, Atmos. Chem. Phys., 8, 5715-5729, 2008.

625 Stolzenburg M.R. and McMurry P.H.: Equations governing single and tandem DMA configurations and
626 a new lognormal approximation to the transfer function, Aerosol Sci. Tech., 42, 421-432, 2008.

627   Stolzenburg M.R. and McMurry P.H.: TDMAFIT user's manual, University of Minnesota, Department
628   of Mechanical Engineering, Particle Technology Laboratory, Minneapolis, 1-61, 1988.
629   Sun Y., Chen C., Zhang Y., Xu W., Zhou L., Cheng X., Zheng H., Ji D., Jie L. and Xiao T.: Rapid
630   formation and evolution of an extreme haze episode in Northern China during winter 2015, Sci. Rep.,
631   6, 2016a.
632   Sun Y., Wang Z., Wild O., Xu W., Chen C., Fu P., Du W., Zhou L., Zhang Q. and Han T.: "APEC Blue":
633   Secondary Aerosol Reductions from Emission Controls in Beijing, Sci. Rep., 6, 2016b.
634   Swietlicki E., Hansson H.C., HÄMeri K., Svenningsson B., Massling A., McFiggans G., McMurry P.H.,
635   PetÄJÄ T., Tunved P., Gysel M., Topping D., Weingartner E., Baltensperger U., Rissler J.,
636   Wiedensohler A. and Kulmala M.: Hygroscopic properties of submicrometer atmospheric aerosol
637   particles measured with H-TDMA instruments in various environments—a review, Tellus B, 60, 432-
638   469, doi:10.1111/j.1600-0889.2008.00350.x, 2008.
639   Tan H., Liu L., Fan S., Li F., Yin Y., Cai M. and Chan P.W.: Aerosol optical properties and mixing state
640   of black carbon in the Pearl River Delta, China, Atmos. Environ., 131, 196-208,
641   doi:10.1016/j.atmosenv.2016.02.003, 2016.
642   Tan H., Xu H., Wan Q., Li F., Deng X., Chan P.W., Xia D. and Yin Y.: Design and application of an
643   unattended multifunctional H-TDMA system, J. Atmos. Ocean. Tech., 30, 1136-1148, 2013a.
644   Tan H., Yin Y., Gu X., Li F., Chan P.W., Xu H., Deng X. and Wan Q.: An observational study of the
645   hygroscopic properties of aerosols over the Pearl River Delta region, Atmos. Environ., 77, 817-826,
646   2013b.
647   Tao W.K., Chen J.P., Li Z., Wang C. and Zhang C.: Impact of Aerosols on Convective Clouds and
648   Precipitation, Rev. Geophys., 50, 1-62, 2012.
649   Wang T., Nie W., Gao J., Xue L.K., Gao X.M., Wang X.F., Qiu J., Poon C.N., Meinardi S., Blake D.,
650   Wang S.L., Ding A.J., Chai F.H., Zhang Q.Z. and Wang W.X.: Air quality during the 2008 Beijing
651   Olympics: secondary pollutants and regional impact, Atmos. Chem. Phys., 10, 7603-7615, 2010.
652   Wang Y., Zhang Q., Jiang J., Zhou W., Wang B., He K., Duan F., Zhang Q., Philip S. and Xie Y.:
653   Enhanced sulfate formation during China's severe winter haze episode in January 2013 missing from
654   current models, Journal of Geophysical Research Atmospheres, 119, 2014.
655   Wehner B., Berghof M., Cheng Y.F., Achtert P., Birmili W., Nowak A., Wiedensohler A., Garland R.M.,
656   Pöschl U. and Hu M.: Mixing state of nonvolatile aerosol particle fractions and comparison with light
657   absorption in the polluted Beijing region, Journal of Geophysical Research Atmospheres, 114, D2,
658   2009.
659   Wehner B., Birmili W., Ditas F., Wu Z., Hu M., Liu X., Mao J., Sugimoto N. and Wiedensohler A.:
660   Relationships between submicrometer particulate air pollution and air mass history in Beijing, China,
661   2004-2006, Atmos. Chem. Phys., 8, 6155-6168, 2008.
662   Wiedensohler A.: An approximation of the bipolar charge distribution for particles in the submicron size
663   range, J. Aerosol Sci., 19, 387-389, 1988.
664   Wu G.X., Li Z.Q., Fu C.B., Zhang X.Y., Zhang R.Y., Zhang R.H., Zhou T.J., Li J.P., Li J.D. and Zhou
665   D.G.: Advances in studying interactions between aerosols and monsoon in China, Science China Earth
666   Science, 59, 1-16, 2016.
667   Wu Z.J., Zheng J., Shang D.J., Du Z.F., Wu Y.S., Zeng L.M., Wiedensohler A. and Hu M.: Particle
668   hygroscopicity and its link to chemical composition in the urban atmosphere of Beijing, China, during
669   summertime, Atmos. Chem. Phys., 16, 1123-1138, 2016.
670   Ye X., Ma Z., Hu D., Yang X. and Chen J.: Size-resolved hygroscopicity of submicrometer urban

671   aerosols in Shanghai during wintertime, Atmos. Res., 99, 353-364,
672   doi:10.1016/j.atmosres.2010.11.008, 2011.

673 Zhang F., Li Y., Li Z., Sun L., Li R., Zhao C., Wang P., Sun Y., Liu X., Li J., Li P., Ren G. and Fan T.:
674   Aerosol hygroscopicity and cloud condensation nuclei activity during the AC[3]Exp campaign:
675   implications for cloud condensation nuclei parameterization, Atmos. Chem. Phys., 14, 13423-13437,
676   doi:10.5194/acp-14-13423-2014, 2014.

677 Zhang F., Li Z., Li Y., Sun Y., Wang Z., Li P., Sun L., Wang P., Cribb M., Zhao C., Fan T., Yang X.
678   and Wang Q.: Impacts of organic aerosols and its oxidation level on CCN activity from measurement
679   at a suburban site in China, Atmos. Chem. Phys., 16, 5413-5425, doi:10.5194/acp-16-5413-2016, 2016.

680 Zhang S.L., Ma N., Kecorius S., Wang P.C., Hu M., Wang Z.B., Größ J., Wu Z.J. and Wiedensohler A.:
681   Mixing state of atmospheric particles over the North China Plain, Atmos. Environ., 125, 152-164,
682   doi:10.1016/j.atmosenv.2015.10.053, 2016.

683 Zhao J., Du W., Zhang Y., Wang Q., Chen C., Xu W., Han T., Wang Y., Fu P., Wang Z., Li Z. and Sun
684   Y.: Insights into aerosol chemistry during the 2015 China Victory Day parade: results from
685   simultaneous measurements at ground level and 260 m in Beijing, Atmos. Chem. Phys., 17, 3215-
686   3232, doi:10.5194/acp-17-3215-2017, 2017.

687

688

689

690 **Table 1.** Summary of size-resolved mean κ, the κ-PDF growth spread factor ($\sigma_{\kappa\text{-PDF}}$),

691 size-resolved mean SF during the selected three periods, and the change in percentage

692 of κ and SF during the control Clean1 period compared with the non-control Clean2

693 period.

		40 nm	80 nm	110 nm	150 nm	200 nm	300 nm
	κ	0.10±0.05	0.11±0.06	0.15±0.07	0.20±0.10	0.25±0.12	—
Clean1	$\sigma_{\kappa\text{-PDF}}$	0.08±0.03	0.10±0.03	0.12±0.03	0.14±0.03	0.15±0.04	—
	SF	0.55±0.08	0.60±0.07	0.64±0.06	0.66±0.05	0.67±0.05	0.70±0.06
	κ	0.14±0.06	0.17±0.08	0.20±0.10	0.24±0.12	0.28±0.13	—
Clean2	$\sigma_{\kappa\text{-PDF}}$	0.11±0.04	0.13±0.03	0.15±0.03	0.17±0.03	0.19±0.04	—
	SF	0.60±0.06	0.66±0.07	0.70±0.07	0.72±0.07	0.74±0.06	0.78±0.06

	κ	0.16±0.08	0.24±0.08	0.30±0.09	0.36±0.10	0.42±0.12	—
Pollution	$\sigma_{\kappa\text{-PDF}}$	0.12±0.02	0.13±0.02	0.14±0.02	0.14±0.0.02	0.15±0.04	—
	SF	0.65±0.06	0.65±0.06	0.65±0.05	0.65±0.05	0.65±0.06	0.66±0.07
$\dfrac{(\text{Clean1} - \text{Clean2})}{\text{Clean2}}$	κ	-32.0 %	-31.9 %	-26.1 %	-17.5 %	-8.5 %	—
	SF	-7.5 %	-9.4 %	-9.2 %	-8.7 %	-10.1 %	-10.5 %
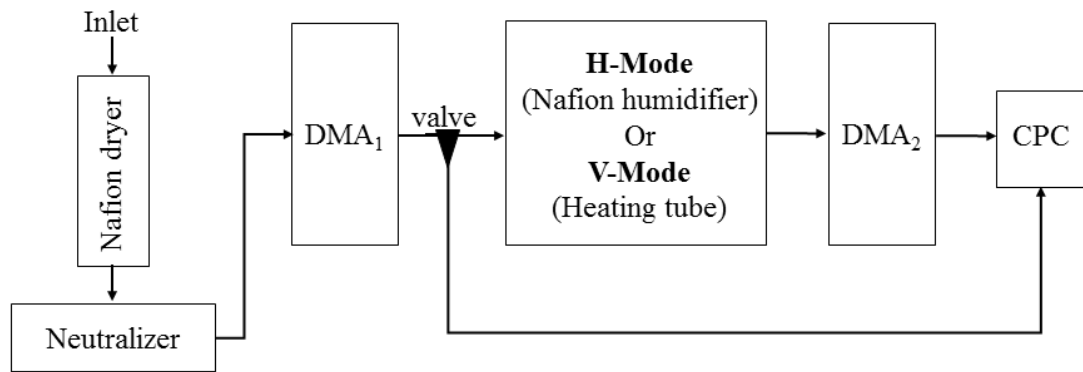
Figure 1. A schematic diagram of the hygroscopic and volatile tandem differential mobility analyzer (H/V-TDMA).
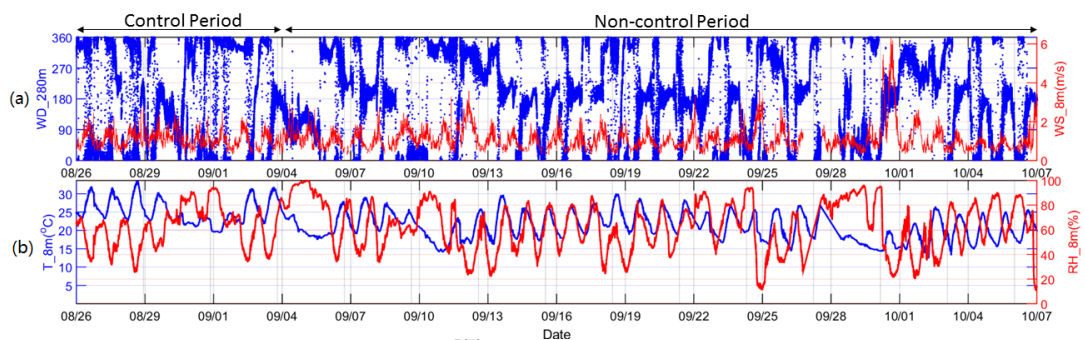
Figure 2. Time series of **(a)** wind direction at 280 m (in blue) and wind speed at 8 m (in red), and **(b)** ambient temperature at 8 m (in blue) and relative humidity at 8 m (in red) during the control and non-control periods.

Figure 3. Time series of **(a)** 10–400 nm aerosol mass concentration (PM$_{10-400 \text{ nm}}$) (assuming that the aerosol density is 1.6 g cm^{-3}), hygroscopicity parameter κ distributions (κ-PDF) for **(b)** 40-nm and **(c)** 150-nm particles at RH = 90 %, and volatile shrink factor distributions (SF-PDF) for **(d)** 40-nm and **(e)** 150-nm particles at T = 300°C.

Figure 4. Diurnal variation in mobility diameter (D$_p$) 10–400 nm particles **(a)** number concentration (N$_{10-400 \text{ nm}}$) and **(b)** mass concentration (PM$_{10-400 \text{ nm}}$) for the Clean1 (in

714   red), Clean2 (in green), and Pollution (in blue) cases.
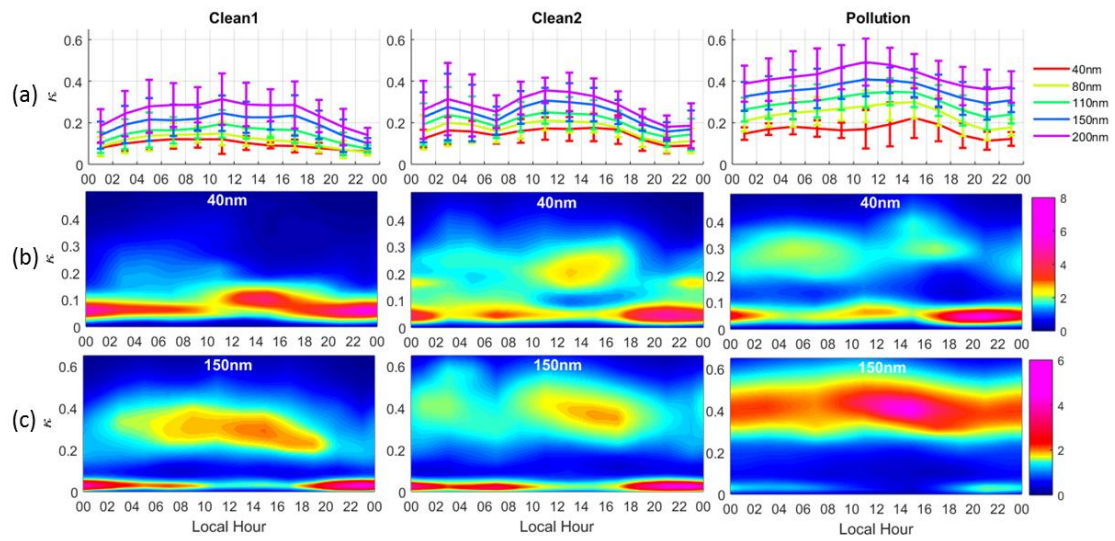
716   **Figure 5.** Diurnal variations in **(a)** mean κ (κ$_{mean}$) for different mobility diameters, **(b)**

717   κ-PDF for particles with D$_p$ equal to 40 nm, and **(c)** κ-PDF for particles with D$_p$ equal

718   to 150 nm during the Clean1, Clean2, and Pollution periods.
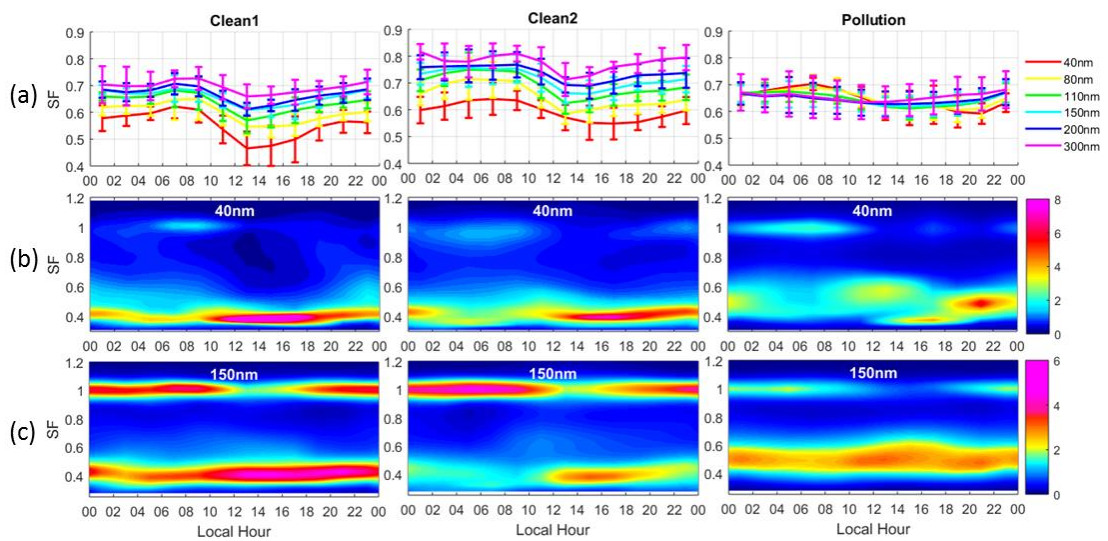
720   **Figure 6.** Diurnal variation of **(a)** mean SF (SF$_{mean}$) for different mobility diameters,

721   **(b)** SF-PDF for particles with D$_p$ equal to 40 nm, and **(c)** SF-PDF for particles with D$_p$

722   equal to 150 nm during the Clean1, Clean2, and Pollution periods.

723
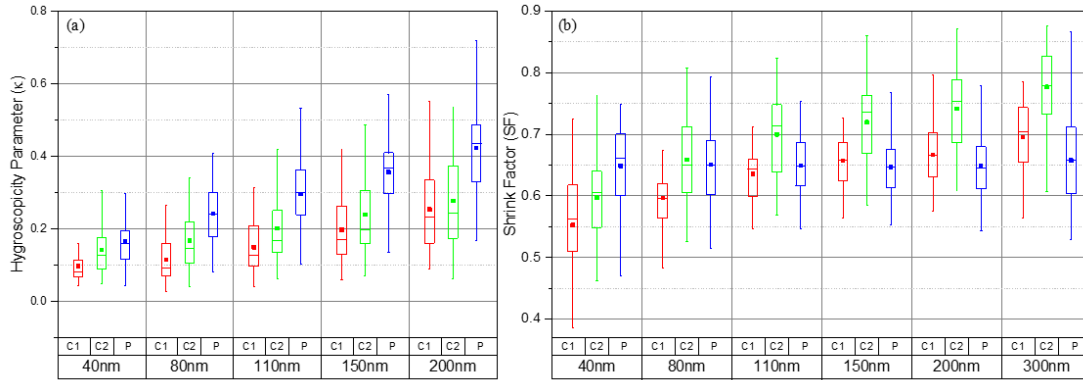
Figure 7. Size-resolved **(a)** κ and **(b)** SF during Clean1 (C1), Clean2 (C2), and

Pollution (P) periods. The figure shows the mean κ or SF (solid square markers) with

boxes showing the 25th, 50th, and 75th percentiles. The extremities show the 5th and

95th percentiles.

728
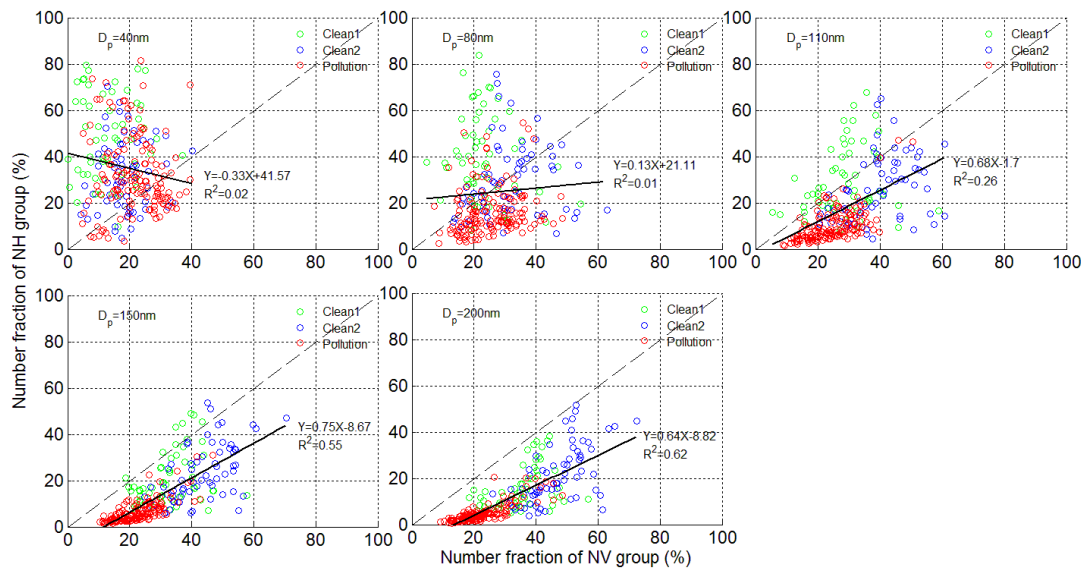
Figure 8. Comparisons between the number fractions of the nearly-hydrophobic

group (NF_{NH}) and the non-volatile group (NF_{NV}) for the Clean1 (in green), Clean2 (in

blue), and Pollution (in red) periods.

732